International Journal of Thermal Sciences 187 (2023) 108174

Contents lists available at ScienceDirect

International Journal of Thermal Sciences

journal homepage: www.elsevier.com/locate/ijts

Localized coupling effects and multiphysics modeling for the laser ablation behavior of composite structure subjected to high-speed airflow

Ruixing Wang [a,b], Zhe Wang [a,b], Te Ma [a,b], Wu Yuan [a,b], Yue Cui [a,b], Hongwei Song [a,b,*]

[a] Key Laboratory for Mechanics in Fluid Solid Coupling Systems, Institute of Mechanics, Chinese Academy of Sciences, Beijing, 100190, China
[b] School of Engineering Science, University of Chinese Academy of Science, Beijing, 100049, China

ARTICLE INFO

Keywords:
Localized coupling effects
Laser ablation behavior
High-speed airflow
Multiphysics modeling
Pit flow regimes

ABSTRACT

When the composite structure is subjected to high-power laser irradiation and high-speed airflow, its ablation behavior presents significant localized characteristics and strong coupling effect. In this work, a coupled fluid-thermal-ablation model is developed to quantitatively investigate the localized coupling effects. Here a loosely coupled scheme with second order temporal accuracy is utilized to improve the coupling efficiency, and a high-quality mesh reconstruction method combining the Arbitrary Lagrange-Euler (ALE) algorithm and Radial Basis Function (RBF) interpolation algorithm is established to capture the moving boundary of the localized ablation pit with large deformation. The model is validated by simulating the laser ablation behavior of C/SiC composite plate subjected to the hypersonic airflow, and the predicted ablation pit profile shows a good agreement with the available experimental result. Analytical results show that as the evolution of the localized asymmetric ablation pit induces transformation of the flow regime from a closed pit flow to an open pit flow. Moreover, the flow regime transition would remarkably alter the localized flow characteristics, including the local static pressure and dynamic pressure, which in turn significantly affects the sublimation and mechanical erosion rates of C/SiC composite plate, respectively.

1. Introduction

In recent years, the laser induced ablation characteristics of composite structures under the high-speed airflow have drawn broad attention with the widely application of the high-power laser technology in manufacturing [1], welding [2] and directed-energy weapon [3]. Generally, the ablation behaviors of composite structures refer to the internal physico-chemical transformation in material, which may involve oxidation, sublimation, melting, pyrolysis and mechanical erosion [4,5]. The laser ablation processes of different composite materials in the static environment have been intensively researched through experimental study [6–9] and numerical analysis [10–13]. However, recent literature has proved that the laser ablation behavior in the high-speed airflow is significantly different from that in the static environment due to the strong localized coupling effects [14–17]. On the one hand, the high-speed airflow influences the ablation behavior in many ways, including: (a) forced convection heat transfer for the structural heat conduction [18]; (b) concentrations of the gas components for the oxidation reaction [19,20]; (c) aerodynamic pressure for the sublimation and melting process [21]; (d) aerodynamic surface shear for the mechanical erosion process [21,22]. On the other hand, the localized ablation behavior, including ablation morphology, wall temperature, ablation products et al., will influence the airflow characteristics in turn. Due to the complex localized coupling effects, the laser ablation mechanism for the target subjected to high-speed airflow has not been fully revealed.

Recently, the issue has been primarily researched through the experiments. Nan et al. [23] investigated the characteristics of plumes when the laminated CFRP composite is subjected to the laser irradiation and tangential airflow or nitrogen gas flow at the speed of 55 m/s. Wang et al. [14] and Wang et al. [15] analyzed the effects of Mach 2.0 and 6.0 airflow on the laser ablation behavior of the C/SiC composite, respectively. Nevertheless, as being influenced by so many factors, including the laser parameters, the structural parameters, the flow conditions et al., it is impossible to cover all the parameter combinations by experimental investigation. Therefore, to fully uncover the localized coupling effects, developing reliable numerical analysis model has become one of the most important issues in this area.

* Corresponding author. Key Laboratory for Mechanics in Fluid Solid Coupling Systems, Institute of Mechanics, Chinese Academy of Sciences, Beijing, 100190, China.
E-mail address: songhw@imech.ac.cn (H. Song).

https://doi.org/10.1016/j.ijthermalsci.2023.108174
Received 19 May 2022; Received in revised form 2 December 2022; Accepted 18 January 2023
Available online 30 January 2023

Generally, the prediction of the laser ablation behavior in high-speed airflow is a typical fluid-thermal-structural-ablation coupling problem. Actually, massive research has been conducted on the numerical modeling and solution for the traditional coupling systems. It is well acknowledged that a multifield coupling problem is well solved by utilizing a partitional loosely coupling approach [24], in which separate solvers are used to compute the fluid, thermal, structural responses, and coupling information is exchanged at the interfaces. Over the past few decades, the strategy was extensively researched on solution algorithm to improve the efficiency [25–28], and has been widely applied in high-speed aircraft design to acquire the fluid-thermal-structural coupling responses of the target in hypersonic airflow [29–34]. Moreover, researchers incorporated the ablation model into the coupling analysis to predict the aerodynamic ablation behavior of the thermal protection systems in reentry environment [35–39]. All these simulations could provide certain reference to numerical analysis of the laser ablation behavior of composite structures in high-speed airflow.

However, compared with the aerodynamic ablation behavior, the laser ablation behavior in high-speed airflow is distinctly different due to the localized coupling characteristics, which make the ablation behavior of composite structures more complicated and bring new challenges to the numerical methods.

(1) The evolution of the localized ablation pit induces significant changes of the flow characteristics, even the flow pattern may alter [17], which causes strong interaction effects between ablation and airflow. In this circumstance, efficient coupling framework comprehensively considering laser irradiation, high speed air flow, material thermal and ablation response, gas-surface interaction as well as moving boundary need to be established to obtain the localized multiphysics responses.
(2) In contrast with the global surface degradation that occurs in the aerodynamic ablation, the localized ablation pit with large deformation is formed in the laser ablation due to the high heat flux around the laser irradiation region. In this case, more powerful mesh deformation methods are needed to capture the moving ablation interface in the numerical analysis.

In view of all above statements, improved numerical analysis methods are needed to carefully reveal the localized coupling effects between the high-speed airflow and laser ablation behavior. Notwithstanding, this is a relatively new research field, studies on which are still rare at present. Consequently, the focus of the present paper is set on the construction and efficient solution for the coupled multifield model regarding the localized ablation behavior of composite structure subjected to laser irradiation and high-speed airflow. Numerical cases about the laser ablation behavior of C/SiC composite plate subjected to the hypersonic flow is conducted for demonstration. The purpose of the work is to gain an insight into the distinctive localized coupling features of the laser behavior in the high-speed airflow.

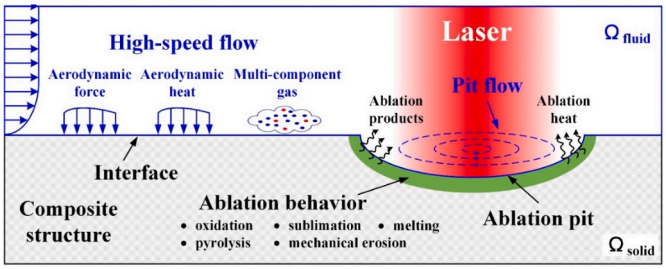

Fig. 1. Illustration of laser ablation behavior subjected to high-speed airflow.

2. Description of the localized multiphysics process

As illustrated in Fig. 1, the laser behavior of composite structure subjected to high-speed airflow is a typical localized multiphysics process, which involves several physical phenomena, including laser beam irradiation, structural heat transfer, multi-mechanism ablation behavior, high-speed airflow, localized pit flow, as well as the fluid-thermal-structural-ablation interactions between fluid domain and solid domain.

The localized multiphysics process can be further divided into four disciplines: fluid flow in the fluid domain, heat transfer, structure, and ablation in the solid domain. According to the interactions of different disciplines, the coupling model can be characterized in Fig. 2. Apparently, strong two-way coupling relationships between different disciplines exist and the coupling quantities in the four disciplines can be respectively classified as follows.

(1) **Fluid flow:** aerodynamic force F_f, aerodynamic heat q_f, and concentrations of the gas components C_g;
(2) **Heat transfer:** structural wall temperature T_w and body temperature T_b;
(3) **Structure:** structural wall deformation D_w and body deformation D_b;
(4) **Ablation:** ablation deformation D_a, ablation products Pr_a and reaction heat q_{ar}.

Note that, for one thing, the structural deformation only has weak effect on structural heat transfer and ablation behaviors; for another, compared with the noticeable morphology change caused by material ablation, the structural deformation of composite material is always small enough to be neglected [40]. Therefore, only the fluid-thermal-ablation coupling model is established to simplify the analysis in the paper.

3. Numerical models for the localized thermal-fluid-ablation coupling analysis

To model the localized coupling behaviors, the computational fluid dynamic (CFD) analysis is conducted to acquire the fluid flow response, the computational solid dynamic (CSD) analysis is implemented to calculate the structural thermal response, as well as the finite rate ablation model is utilized to predict the ablation behavior. Moreover, the mass and energy balance relationship on the interface is established to couple the three disciplines.

3.1. Fluid flow model

To predict the complex flowfield over an ablating surface, the viscous compressible flow is described by the conservation equations of mass, momentum, energy The governing equations are written as follows:

$$\frac{\partial \rho}{\partial t} + \nabla \cdot (\rho \boldsymbol{v}) = 0 \tag{1}$$

$$\frac{\partial (\rho \boldsymbol{v})}{\partial t} + \nabla \cdot (\rho \boldsymbol{v}\boldsymbol{v}) + \nabla p = \nabla \cdot \bar{\bar{\tau}} \tag{2}$$

$$\frac{\partial (\rho E)}{\partial t} + \nabla \cdot [\boldsymbol{v}(\rho E + p)] = \nabla \cdot \left[\lambda \nabla T - \sum_i h_i \boldsymbol{J}_i + (\bar{\bar{\tau}} \cdot \boldsymbol{v}) \right] \tag{3}$$

where ρ is the density, $\boldsymbol{v}$ is the velocity vector, p is the pressure, $\bar{\bar{\tau}}$ is the stress tensor, T is the temperature, E is the specific internal energy, λ is the thermal conductivity, respectively.

The Shear-Stress Transport (SST) k-ω model is adopted to characterize the turbulence, which is more reliable than both the standard and baseline k-ω models by additionally accounting for the transport of the

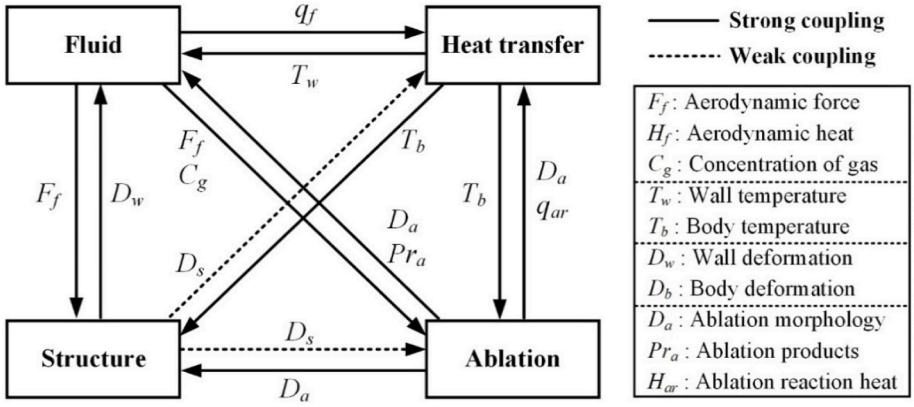

Fig. 2. Fluid-thermal-structural-ablation interactions of multiphysics.

turbulence shear stress in the turbulent viscosity. For the computation of high-speed flow, all the governing equations are solved simultaneously using the finite volume approach by ANSYS Fluent 16.0 [41].

3.2. Heat transfer model

Based on the law of Fourier heat conduction and energy conversation, the general governing equations of the transient structural heat transfer in material can be expressed as:

$$\rho_s c_s \frac{\partial T_s}{\partial t} = \frac{\partial}{\partial x_i}\left(k_s \frac{\partial T_s}{\partial x_i}\right) + \dot{Q} + q_\Gamma \quad (i = 1, 2, 3) \tag{4}$$

where t is the time, T_s is the structural temperature, ρ_s is the structural density, c_s is the structural specific heat, k_s is the structural thermal conductivity, $\dot{Q}$ is the volumetric heating source in a solid, and q_Γ is the heat flux imposed on the boundary.

In this study, the finite element method (FEM) is used to discretize Eq. (4), and then the discretized matrix formulation can be rewritten as:

$$[\boldsymbol{C}_T]\{\dot{\boldsymbol{T}}\} + [\boldsymbol{K}_T]\{\boldsymbol{T}\} = \{\boldsymbol{Q}\} \tag{5}$$

here, $[\boldsymbol{C}]$, $\{\boldsymbol{T}\}$, $[\boldsymbol{K}]$, $\{\boldsymbol{Q}\}$ denote the thermal capacitance matrix, temperature vector, thermal conductivity matrix, and nodal heat load vector, respectively.

In this work, Eq. (5) is discretized in time utilizing the unconditional stable implicit backward Euler method, which is second-order accurate and can be represented by

$$[\boldsymbol{C}_T]^m \frac{\{\boldsymbol{T}\}^m - \{\boldsymbol{T}\}^{m-1}}{\Delta t_T} + [\boldsymbol{K}_T]^m \{\boldsymbol{T}\}^m = \{\boldsymbol{Q}\}^m \tag{6}$$

where m and Δt_T are the thermal time step counter and time step, respectively. And the Newton's method is adopted as the numerical technique for solving the nonlinear equilibrium equations.

3.3. Laser ablation model for composite material

The energy accumulation caused by the laser irradiation induces a local high temperature of solid material. When further coupled with high-speed flow, the server environment leads to complex thermal-mechanical ablation behavior. For the different types of composite materials, the surface ablation mechanism may involve chemical reaction, sublimation, melting, thermomechanical erosion and so on. The finite rate ablation model of composite material can be introduced to acquire the recession rate of material surface. In the model, the total ablation rate normal to the surface r_{total} is assumed to be a linear superposition of the rates of different independent ablation processes:

$$r_{total} = r_c + r_s + r_m + r_e \tag{7}$$

where r_c, r_s, r_m, r_e denote the recession rates of chemical reaction, sublimation, melting, thermomechanical erosion of the composite structure, respectively.

The recession rates are determined by the ablation model in Ref. [40]. It quantitatively describes the theoretical relationships between recession rates and flow parameters. In brief, the relationships can be expressed as

$$\begin{cases} r_c = r_c\left(\alpha/c_p, C_g^i\right) \\ r_s = r_s\left(\alpha/c_p, p_e\right) \\ r_m = r_m(p_v) \\ r_e = r_e(p_v) \end{cases} \tag{8}$$

where α/c_p is the heat transfer coefficient, p_e is the local pressure, p_v is the dynamic pressure, which is defined as

$$p_v = \frac{1}{2}\rho_e v_e^2 \tag{9}$$

where ρ_e and v_e are the density and velocity at the external boundary layer, respectively.

Note that, the explicit expressions of Eq. (9) can be acquired according to the characteristics of certain type of composite structures. For example, a complete description about the ablation model of C/SiC composites is supplied in Appendix A to support the validation case in section 5.

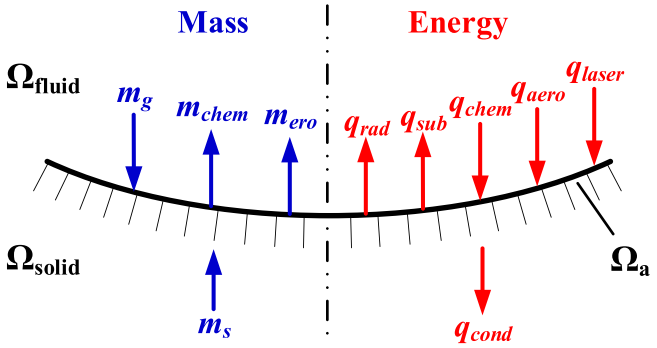

Fig. 3. Mass and energy balances on the coupled ablation surface.

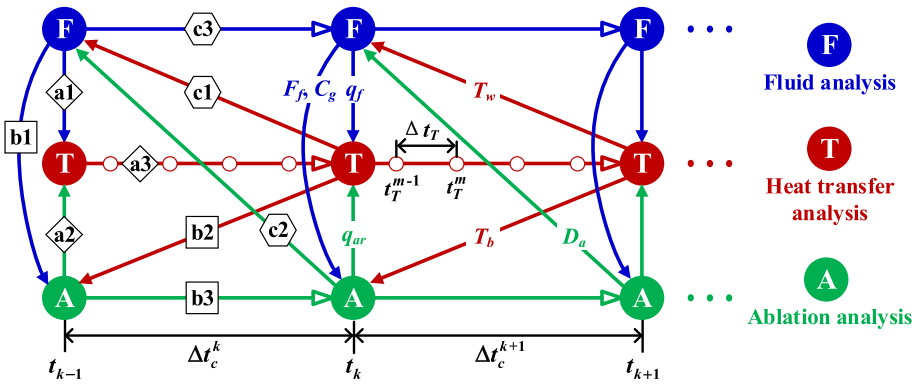

Fig. 4. Loosely coupled strategy over two coupling time steps.

3.4. Mass and energy balances on the ablative surface

As the solid domain and fluid domain interact at the coupled ablative interface Ω_a with mass and energy transport, the general surface mass and energy balances can be illustrated in Fig. 3.

The mass balance for a chemically reacting surface can be written as

$$m_s = m_{chem} + m_{ero} - m_g \tag{10}$$

where m_s is the total mass loss of the solid, m_{chem} is the mass loss caused by the chemical reaction, m_{ero} is the mass loss caused by the thermo-mechanical erosion, m_g is the mass of the consumed gas mass in the overrunning flow.

Meanwhile, the surface energy balance can be expressed as

$$q_{cond} = q_{laser} + q_{aero} + q_{chem} - q_{sub} - q_{rad} \tag{11}$$

where q_{cond} is heat flux conducted into the solid material, q_{laser} is the laser heat flux, q_{aero} is aerodynamic heat flux caused by the high speed flow, q_{chem} is the heat flux caused by the chemical reaction (mainly oxidation and nitridation), q_{sub} is the sublimation heat flux, q_{rad} is the radiative heat flux, which can be calculated as follows:

$$q_{rad} = \varepsilon\sigma_s\left(T_w^4 - T_0^4\right) \tag{12}$$

where ε, T_w and T_0 are the surface emissivity, surface temperature and ambient temperature, respectively, σ_s denotes the Stefan-Boltzmann constant, 5.67×10^{-8} W/(m^2•K^4).

4. Efficient coupling framework for the localized multiphysics process

4.1. Second order temporal accuracy loosely coupling strategy

The ability to exploit the disparity of timescales in solvers is regarded as an advantage of loosely coupled partitioned strategy. It is well known that the characteristic time scale for high-speed airflow to reach the steady state is much always smaller than that of transient structural heat transfer problem [29]. Moreover, the ablation is always considered to occur immediately on the interface [21]. Consequently, to take full advantage of the timescale disparity of the three individual solvers, the quasi-steady models of fluid analysis and ablation analysis, as well as the transient model of heat transfer analysis are adopted.

Based on this, a generalized loosely coupling procedure of fluid-thermal-ablation interactions is presented in Fig. 4. t_{k-1}, t_k, Δt_c are the start, end and step-size of the kth coupling step, respectively; t_T^{m-1}, t_T^m, Δt_T are the start, end and the step-size of the mth heat transfer analysis step in a coupling step, respectively. In this paper, Δt_c and Δt_T are set to be constants, and Δt_c is obviously multiples of Δt_T. Moreover, to guarantee accuracy and efficiency, the extrapolation-based predictors [27, 28] for the coupling quantities between the coupling steps are utilized to maintain the second-order temporal accuracy.

Specifically, the second order temporal accuracy loosely coupling strategy from t_{k-1} to t_k for the three solvers can be described in the following sequence.

Step 1. Heat transfer analysis

(a1). q_f is passed from the fluid solver to the heat transfer solver. As explained in Eq. (6), heat flux at time t_T^m is required to march the thermal solution forward in time. However, q_f^m is not known ahead of the current solution, so a predictive extrapolation is conducted as an estimate. To maintain second-order accuracy, the heat flux is estimated by the central difference method as

$$q_f^m = q_f^{m-1} + \left(q_f^{m-1} - q_f^{m-2}\right) + \mathrm{O}\left(\Delta t_T^2\right) \tag{13}$$

(a2). q_{ar} is passed from the ablation solver to the heat transfer solver. Similarly, q_{ar}^m can be estimated as

$$q_{ar}^m = q_{ar}^{m-1} + \left(q_{ar}^{m-1} - q_{ar}^{m-2}\right) + \mathrm{O}\left(\Delta t_T^2\right) \tag{14}$$

(a3). The transient heat transfer is conducted over Δt_c^k, and the solution time is updated to t_k.

Step 2. Ablation analysis

(b1). In this step, the involving aerodynamic quantities, including p_e, p_v and C_g^j, are passed from the fluid solver to the ablation solver. The aerodynamic quantities are interpolated as

$$\begin{cases} p_e^m = p_e^{m-1} + \left(p_e^{m-1} - p_e^{m-2}\right) + \mathrm{O}\left(\Delta t_T^2\right) \\ p_v^m = p_v^{m-1} + \left(p_v^{m-1} - p_v^{m-2}\right) + \mathrm{O}\left(\Delta t_T^2\right) \\ \left(C_g^j\right)^m = \left(C_g^j\right)^{m-1} + \left[\left(C_g^j\right)^{m-1} - \left(C_g^j\right)^{m-2}\right] + \mathrm{O}\left(\Delta t_T^2\right) \end{cases} \tag{15}$$

(b2). The body temperature T_b, which has been updated at time t_k in the heat transfer solver, is directly passed to the ablation solver;

(b3). The ablation analysis is conducted and the solution time is updated to t_k.

Step 3. Fluid analysis

(c1). T_w, which has been updated at t_k in the thermal solver, is directly passed to the fluid solver;

(c2). D_a, which has been updated at t_k in the ablation solver, is directly passed to the fluid solver;
(c3). The high-speed fluid flow analysis is conducted and the solution time is updated to t_k.

Step 4. Loop

By conducting above steps, the overall solution time considering all the three solvers is updated from t_{k-1} to t_k, which means one coupling time step is accomplished. And the analysis will continue to the next coupling step by repeating Step 1-Step 3 until the total calculation time is reached.

Note that, as there are no subiterations between each coupling time step, a time lag exists between the three solvers. Thus, a proper coupling time step should be chosen in the coupling strategy to ensure the stability and accuracy. As demonstrated in Section 5, study on the effects of the time step needs to be conducted for the specific problem.

4.2. Information exchange on the coupled interface

In the coupling analysis, the fluid mesh and the solid mesh are always different in distribution density, which would lead to the grid mismatching on the coupling interface. Thus, the information exchange should be conducted through an interpolation algorithm. Moreover, along the coupling interface, the continuity conditions of temperature, mass concentration of the gas component, dynamic pressure, as well as the conservation conditions of wall heat flux and local pressure are applied, which can be written as follows:

$$v_s = v_f \tag{16}$$

$$\int_{\Omega_a} V_s ds = \int_{\Omega_a} V_f ds \tag{17}$$

where v_s, v_f and V_s, V_f denote the coupling variables for continuity and conservation on solid and fluid boundaries, respectively.

In this paper, the hybrid interpolation strategy is adopted. On the one hand, the transfer of the variables for continuity is conducted by the inverse distance weight (IDW) interpolation method, which is simple, direct, and computationally efficient, but not interpolation conservative [29]; on the other hand, the transfer of the variables for conservation is carried out by the control surface based interpolation algorithm to ensure the interpolation conservation [32].

4.3. Solid and fluid mesh reconstruction for the localized ablation deformation

Both fluid and solid mesh should be updated after each coupling timestep owning to the significant deformation of coupling interface caused by the local ablation pit. However, the large and irregular deformation would easily result in poor-quality mesh region, and then the traditional ALE technique [35,39,42] is no longer applicable while the local interpolation algorithm is always used. To overcome it, a mesh deformation method combining the Arbitrary Lagrange-Euler (ALE) algorithm and Radial Basis Function (RBF) interpolation algorithm is established.

4.3.1. Solid mesh reconstruction

The ALE adaptive mesh algorithm can maintain a high-quality mesh by allowing the mesh to move independently of the material. Generally, ALE meshing consists of two fundamental tasks: reconstructing new mesh, and remapping solution variables from the old mesh to the new mesh.

(1) Reconstructing new mesh

The RBF interpolation method has been extensively applied in mesh deformation for its advantages on efficiency, mesh quality and globality [43–45]. The formulation of RBF interpolation can be generally expressed as

$$g(\mathbf{x}) = \sum_{i=1}^{N} \alpha_i \varphi(\|\mathbf{x} - \mathbf{x}_i\|) \tag{18}$$

where $\mathbf{X} = \{\mathbf{x}_1, \mathbf{x}_2, \cdots, \mathbf{x}_N\}$ denotes the position of the node in the known node set, also called the control point, and the corresponding scalar value of which is $\mathbf{g} = \{g_1, g_2, \cdots, g_N\}$. $g(\mathbf{x})$ denote the functional value of the new node, whose position is $\mathbf{x}$. $\|\mathbf{x} - \mathbf{x}_i\|$ is the Euclidean distance from the new node to the known node. α_i is the coefficient determined by the following definite conditions:

$$g(\mathbf{x}_i) = g_i, i = 1, 2, \cdots, N \tag{19}$$

φ is basis function. Specially, to increase the computational efficiency, the compactly supported RBF, which can strictly limit the influence within a support region, is adopted. In this work, the form of Wendland's C2 is used as the basis functions, which can be expressed as

$$\varphi(\xi) = \begin{cases} (1-\xi)^4(4\xi+1) & \xi < 1 \\ 0 & \xi \geq 1 \end{cases} \tag{20}$$

where $\xi = \|\mathbf{x} - \mathbf{x}_i\|/r_0$ and r_0 is the compactly supported radius.

Based on the above, assume that the number and original location of the solid nodes on the coupling surface are respectively N_s^{Sur} and $\mathbf{x}_{si}^{Sur}, i = 1, 2, \cdots, N_s^{Sur}$. The deformation of the nodes is known as $(\mathbf{D}_s^{Sur})^T = [D_{s1}^{Sur}\ D_{s2}^{Sur} \cdots D_{sN_s^{Sur}}^{Sur}]$, which is known after solving the ablation model. Then, Eq. (20) can be rewritten as

$$\mathbf{D}_s = \mathbf{\Phi}_{ss}\boldsymbol{\alpha} \tag{21}$$

where

$$\boldsymbol{\alpha} = \begin{bmatrix} \alpha_1 & \alpha_2 & \cdots & \alpha_{N_s^{Sur}} \end{bmatrix}, \mathbf{\Phi}_{ss} = \begin{bmatrix} \varphi_{s11} & \varphi_{s12} & \cdots & \varphi_{s1N_s^{Sur}} \\ \varphi_{s21} & \varphi_{s22} & \cdots & \varphi_{s2N_s^{Sur}} \\ \vdots & \vdots & \ddots & \vdots \\ \varphi_{sN_s^{Sur}1} & \varphi_{sN_s^{Sur}2} & \cdots & \varphi_{sN_s^{Sur}N_s^{Sur}} \end{bmatrix}, \varphi_{sij} = \varphi\left(\left\|\mathbf{x}_{si}^{Sur} - \mathbf{x}_{sj}^{Sur}\right\|\right) \left(i, j = 1, 2, \cdots, N_s^{Sur}\right) \tag{22}$$

Obviously, the coefficient $\boldsymbol{\alpha}$ can be obtained by solving the following equation:

$$\boldsymbol{\alpha} = \mathbf{\Phi}_{ss}^{-1}\mathbf{D}_s \tag{23}$$

Subsequently, for the nodes inside the solid domain, whose number and location are respectively N_s^{Vol} and $\mathbf{x}_{si}^{Vol}, i = 1, 2, \cdots, N_s^{Vol}$, the deformation $\mathbf{D}_s^{Vol} = [D_{s1}^{Vol}\ D_{s2}^{Vol} \cdots D_{sN_s^{Vol}}^{Vol}]$ can be determined by

$$\mathbf{D}_s^{\mathrm{Vol}} = \mathbf{A}_{\mathrm{S\_to\_V}}\boldsymbol{\alpha} = \mathbf{A}_{\mathrm{S\_to\_V}}\boldsymbol{\Phi}_{ss}^{-1}\mathbf{D}_s^{\mathrm{Sur}} \tag{24}$$

where

$$\mathbf{A}_{\mathrm{S\_to\_V}} = \begin{bmatrix} \varphi_{\mathrm{S1,V1}} & \varphi_{\mathrm{S1,V2}} & \cdots & \varphi_{\mathrm{S1,V}N_s^{\mathrm{Vol}}} \\ \varphi_{\mathrm{S2,V1}} & \varphi_{\mathrm{S2,V2}} & \cdots & \varphi_{\mathrm{S2,V}N_s^{\mathrm{Vol}}} \\ \vdots & \vdots & \ddots & \vdots \\ \varphi_{\mathrm{S}N_s^{\mathrm{Sur}},\mathrm{V1}} & \varphi_{\mathrm{S}N_s^{\mathrm{Sur}},\mathrm{V2}} & \cdots & \varphi_{\mathrm{S}N_s^{\mathrm{Sur}},\mathrm{V}N_s^{\mathrm{Vol}}} \end{bmatrix}, \quad \varphi_{Si,\mathrm{V}j} = \varphi\left(\left\|\mathbf{x}_{si}^{\mathrm{Sur}} - \mathbf{x}_{sj}^{\mathrm{Vol}}\right\|\right) \quad \left(i = 1,2,\cdots,N_s^{\mathrm{Sur}}; j = 1,2,\cdots,N_s^{\mathrm{Vol}}\right) \tag{25}$$

Then, the location of the nodes inside the solid domain after deformation can be updated as.

$$\left(\mathbf{x}_s^{\mathrm{Vol}}\right)^{\mathrm{new}} = \left(\mathbf{x}_s^{\mathrm{Vol}}\right)^{\mathrm{old}} + \mathbf{D}_s^{\mathrm{Vol}} \tag{26}$$

After that, the deformed mesh can be easily regenerated by only updating the node location while the mesh connectivity is always unchanged.

(2) Remapping solution variables

After the deformed solid mesh is acquired, the solution variable, namely the body temperature is subsequently remapped from the old mesh to the new mesh. In the paper, the body temperature is remapped by the RBF interpolation method as

$$\mathbf{T}_s^{\mathrm{V\_def}} = \mathbf{A}_{\mathrm{V\_to\_V}}\boldsymbol{\Phi}_{ss}^{-1}\mathbf{T}_s^{\mathrm{V\_undef}} \tag{27}$$

where $\mathbf{A}_{\mathrm{v\_to\_v}}^{s}$ and $\boldsymbol{\Phi}_{ss}^{-1}$ are similar to Eqs. (23) and (26), $\mathbf{T}_s^{\mathrm{V\_def}}$ and $\mathbf{T}_s^{\mathrm{V\_undef}}$ are the body temperature of the deformed mesh and undeformed mesh, respectively.

4.3.2. Fluid mesh reconstruction

For the fluid mesh, the deformation of solid boundary $\mathbf{D}_s^{\mathrm{Sur}}$ is considered as the source data to satisfy the compatibility of deformation, and the deformations of the internal nodes inside the fluid domain $\mathbf{D}_f^{\mathrm{Vol}}$ can be similarly calculated as

$$\mathbf{D}_f^{\mathrm{Vol}} = \mathbf{A}_{\mathrm{S\_to\_V}}\boldsymbol{\Phi}_{sf}^{-1}\mathbf{D}_s^{\mathrm{Sur}} \tag{28}$$

where $\mathbf{A}_{\mathrm{S\_to\_V}}$ and $\boldsymbol{\Phi}_{sf}^{-1}$ are similar to Eq. (24).

Then, the location of the nodes after deformation can be updated as

$$\left(\mathbf{x}_f^{\mathrm{Vol}}\right)^{\mathrm{new}} = \left(\mathbf{x}_f^{\mathrm{Vol}}\right)^{\mathrm{old}} + \mathbf{D}_f^{\mathrm{Vol}} \tag{29}$$

where $\mathbf{x}_f^{\mathrm{Vol}}$ denotes the location of the nodes inside the fluid.

After the deformed fluid mesh is acquired, the solution variables are remapped through IDW interpolation method [41].

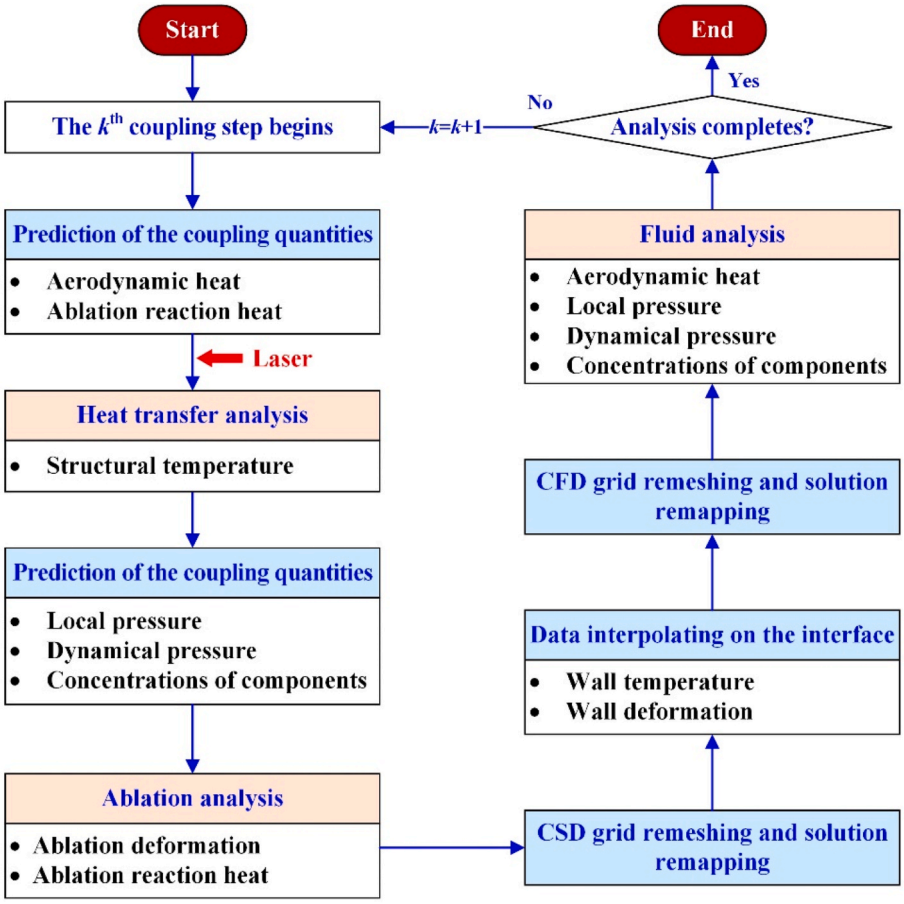

Fig. 5. Flowchart of proposed coupling approach.

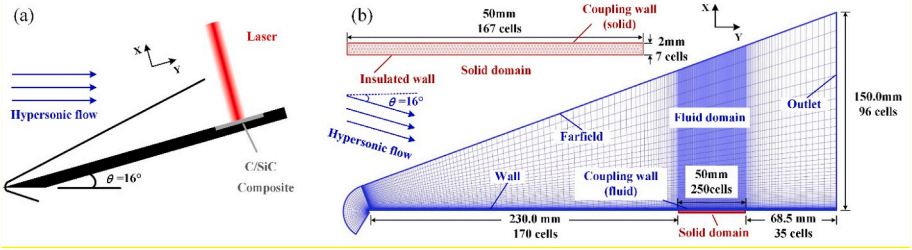

Fig. 6. Illustration of the simulation model. (a) The flat plate model; (b) The computational domain.

Table 1
Freestream conditions.

Property	Symbol	Value
Mach number	Ma	6.0
Density	ρ_g	0.04 kg/m^3
Static temperature	T_{static}	222.4 K
Static pressure	p_{static}	2550.0 Pa
Total temperature	T_{total}	1784.0 K
Total pressure	p_{total}	4257 kPa
Angle of attack	β	0°
Mass fractions		
O_2	C_g^1	23%
N_2	C_g^2	77%

4.4. Implementation procedure

In the section, the framework integrating individual discipline solvers, coupling strategy, date exchange, mesh deformation is established for the localized laser ablation behavior in high-speed airflow. The implementation flowchart is illustrated in Fig. 5. Two points need to emphasize here. Firstly, a steady-state fluid computation should be performed before the coupling analysis to initialize the coupled computations. Secondly, given that the framework involves multiple loops of fluid-thermal-ablation analyses, a self-complied program with Python programming language is developed to automatically perform the whole analysis process.

5. Case studies and discussion

In this section, numerical analysis for the laser ablation behavior of C/SiC composite subjected to high-speed airflow, which was experimentally researched in the previous work [15], is conducted. The proposed coupling analysis scheme is firstly validated, and then the localized coupling effects for this case are investigated.

5.1. Description of the coupling CFD/CSD model

Two-dimensional simulation model is established to numerically reproduce the test in Ref. [15]. As shown in Fig. 6 (a), a flat plate for naturally developed turbulent boundary layer is considered and the deflection angle of the flat plate is 16.0°. The front of the C/SiC composite plate, whose size is 50 mm × 2 mm, is located 230 mm along X direction from the leading edge of the flat plate.

The airflow and laser irradiation conditions are identical to the experimental test [15]. The airflow conditions are listed in Table 1. The hypersonic wind tunnel is utilized to approximate the flow conditions as follows: Mach number is 6.0, and the attitude is 25 km. Note that, the total temperature of the high-speed flow is 1784.0 K, which is lower than the dissociation temperature of either O_2 or N_2 [46], thus the chemical reaction inside the boundary lay is ignored. Additionally, the laser irradiation conditions are listed in Table 2, and the heat flux caused by the laser irradiation can be calculated as follows:

Table 2
Laser irradiation parameters.

Property	Symbol	Value
Average laser power	q_a	2.0 kW
Spot radius	r_0	5.0 mm
Distribution	φ	Gaussian
Absorption coefficient	ε	0.62 [47]
Irradiation time	t	4.0 s

Table 3
Material properties of C/SiC composite.

Property	Symbol	Value
Density of fiber	ρ_f	1760.0 kg/m^3
Thermal conductivity of fiber	k_f	42.0 W/(m·K)
Specific heat of fiber	c_f	600.0 J/(kg·K)
Volume fraction of fiber	φ_f	40.0%
Strength of fiber in longitudinal/transverse directions	$\sigma_{f,longi}/\sigma_{f,trans}$	2200/220 MPa
Density of matrix	ρ_m	3190.0 kg/m^3
Thermal conductivity of matrix	k_m	20.0 W/(m·K)
Specific heat of matrix	c_m	700.0 J/(kg·K)
Volume fraction of matrix	φ_m	42.2%
Strength of matrix	σ_m	100.0 MPa
Activation energy of sublimation for C	$E_{C,S}$	6.65 × 10^5 J/mol
Activation energy of sublimation for SiC	$E_{SiC,S}$	8.73 × 10^4 J/mol
Pre-exponential multiplier of oxidation for C	$A_{C,O}$	5.77 × 10^5 kg/m^3•s
Pre-exponential multiplier of oxidation for SiC	$A_{SiC,O}$	10.0 kg/m^3•s
Activation energy of oxidation for C	$E_{C,O}$	1.142 × 10^5 J/mol
Activation energy of oxidation for SiC	$E_{SiC,O}$	9.46 × 10^4 J/mol
Pre-exponential multiplier of thermo-decomposition process for fiber	J_f^0	5.4 × 10^2 kg/m^3•s
Pre-exponential multiplier of thermo-decomposition process for matrix	J_m^0	5.0 × 10^5 kg/m^3•s
Activation energy of thermo-decomposition process for fiber	E_{Af}	5.4 × 10^4 J/mol
Activation energy of thermo-decomposition process for matrix	E_{Am}	8.73 × 10^4 J/mol

Table 4
Grid sensitivity analysis for CFD and CSD model.

Version	CSD model		CFD model		
	Max. grid scale	Total cell numbers	Grid spacing of the first layer	Max. grid spacing along the coupling wall	Total cell numbers
Coarse	0.50 mm	810	4 × 10^{-3} mm	0.40 mm	23370
Medium	0.30 mm	2662	1 × 10^{-3} mm	0.20 mm	41976
Fine	0.15 mm	10040	5 × 10^{-4} mm	0.10 mm	72928

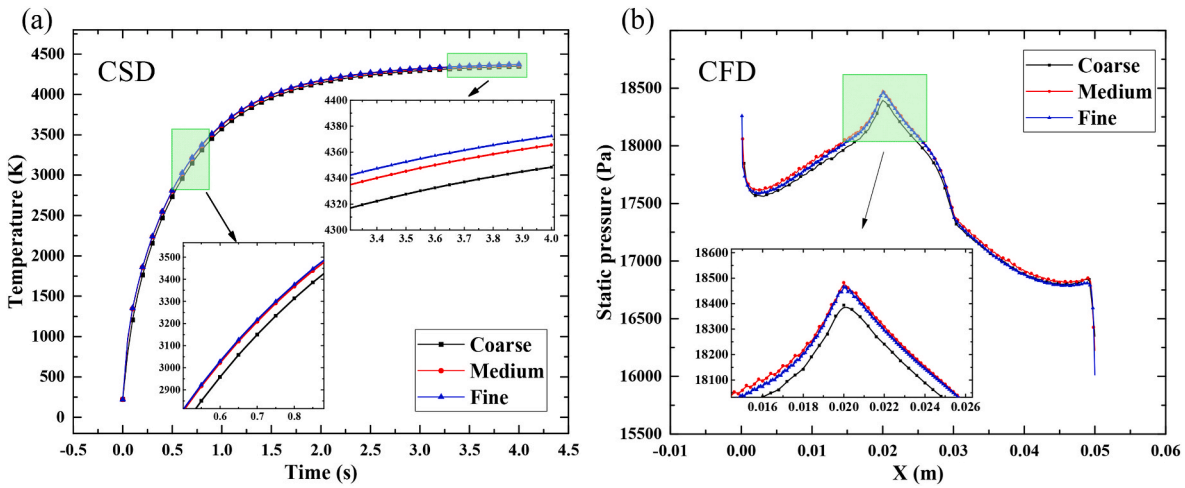

Fig. 7. Results of grid sensitivity analysis. (a) Time evolution of maximum wall temperature for the CSD model; (b) Static pressure along the coupling wall for the CFD model.

$$q_{\text{laser}} = \varepsilon \frac{1}{1-e^{-2}} \frac{q_a}{\pi r_0^2} \exp\left(-2\frac{x^2+y^2}{r_0^2}\right) \tag{30}$$

According to Ref. [5], the C/SiC composite with 2D woven carbon fiber preform was tested. The material properties are listed in Table 3. Moreover, the heterogeneous ablation mechanisms of C/SiC composites are considered: (1) the multi-component thermochemical ablation due to the surface chemical reaction kinetics, including the oxidation, and sublimation of SiC matrix and carbon fiber; (2) the mechanical erosion of SiC matrix and carbon fiber due to the high-speed airflow. The detailed description of the ablation model is supplied in Appendix A. Note that, due to the high intensity heat flux caused by the laser irradiation, the structural temperature would rapidly increase above 3000 K, in this case, the oxidation exerts only a weak influence on the ablation behavior [48]. Therefore, the oxidation model in this paper is simplified by neglecting the interaction between oxidation reaction and boundary layer, which would not affect the reasonability of our analysis.

5.2. Validation of the proposed multiphysics coupling analysis model

5.2.1. Grid sensitivity for CFD/CSD model

As displayed in Fig. 6 (b), the computational domain is subdivided into two zones: fluid domain and solid domain. The grid sensitivity analysis is firstly conducted. Three versions of grid resolutions are listed in Table 4 for both CFD model and CSD model. The transient heat transfer analysis for C/SiC composite under laser irradiation is regarded as a validation case for CSD model. Note that the ablation is ignored here for simplicity. And the aerodynamic performance under the temperature distribution obtained from the heat transfer analysis is considered as the validation case for CFD model. It can be found from Fig. 7 that the grid accuracy of the medium version is sufficient. As a result, for the solid domain, the unstructured mesh consists of 100 cells along the length and 5 cells through the thickness. In the CSD model, the heat flux is prescribed on the coupling surface of the panel, while the other three surfaces are assumed perfectly insulated. For the fluid domain, the grid is constructed with 405 cells in the streamline direction and 96 cells in the normal direction. Specially, the grid scales are refined to 0.25 mm in streamline direction and 1×10^{-3} mm in the normal direction near the coupling wall to accurately capture the near wall phenomena. Thus, $y^+ \sim 1$ near the coupling wall is satisfied and the CFD results are ensured to be grid independent. The CFD model is constrained to three boundary conditions, namely, hypersonic far field, outlet, no slip wall, which indicates that the fluid sticks to the moving wall. And the initial wall

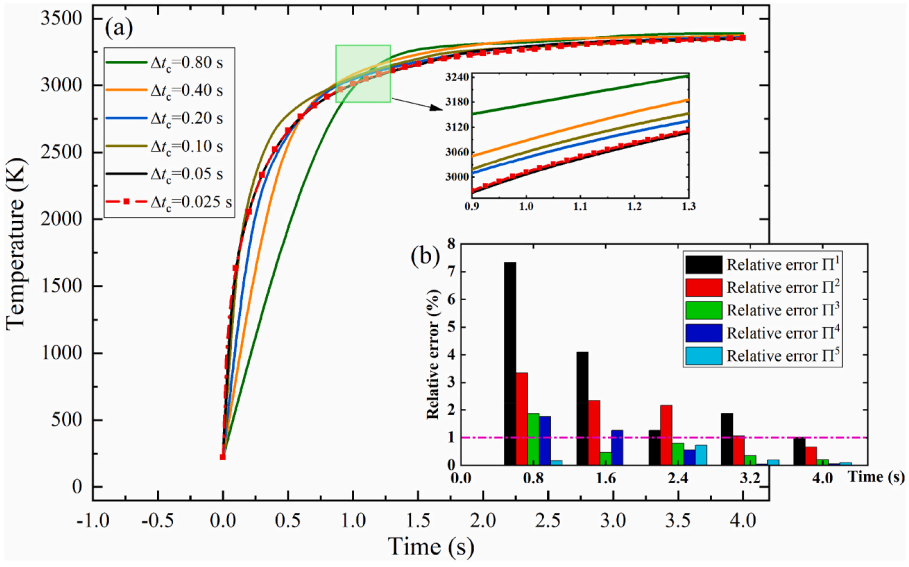

Fig. 8. Effects of coupling time step on the maximum temperature of C/SiC composite.

temperature of is set to be the uniform 222.3 K, which is the static temperature of the freestream.

5.2.2. Effects of coupling time step

In this section, the effects of the coupling time step, which controls the frequency of remeshing the computational domains and updating the boundary conditions, are carefully discussed. For this case, the analysis is performed over a period of 4.0 s, and six levels of coupling time steps are considered, ranging from 0.8 s for the coarsest level to 0.025 s for the finest level:

$$\Delta t_c^i = 0.8 \times \left(\frac{1}{2}\right)^{i-1} \quad (i = 1, \cdots, 6) \tag{31}$$

where i is the time step level between 1 and 6.

Moreover, to qualify the effects, the relative error between the response solved with current time step and that solved with the smallest time step is defined as

$$\Pi^i = \left| \frac{\Psi(\Delta t_c^i) - \Psi(\Delta t_c^6)}{\Psi(\Delta t_c^6)} \right| \quad (i = 1, \cdots, 5) \tag{32}$$

where Π is the relative error, $\Psi(\Delta t_c^i)$ is the response solved with coupling time step Δt_c^i.

The comparisons of the maximum temperature history with different coupling steps are shown in Fig. 8(a), and the corresponding relative errors are illustrated in Fig. 8(b). It can be seen that.

(1) The coupling time step has a significant influence on the temperature rising process. For instance, the relative error of maximum temperature reduces from 7.33% to 0.16% at 0.8 s when Δt_c decreases from 0.8 s to 0.05 s.
(2) When $\Delta t_c = 0.05$ s, the maximum relative error over the time period is 0.71%. Under this circumstance, it could be argued that the solution is stable and converged with this time step.

Therefore, it can be concluded that the proposed coupling analysis method could obtain more accurate solution with the smaller the coupling time step. However, smaller time step means more computational effort. Therefore, to balance the accuracy and efficiency, the coupling time step of 0.05 s is chosen for the following analysis.

5.2.3. Mesh quality during the ablation process

To ensure the accuracy of the analysis results, the mesh quality should be preserved during the ablation process. Fig. 9 depicts the time evolution of mesh quality for both solid and fluid domains based on the proposed mesh construction methods. For the CSD mesh, the minimum angle on the triangular face [42] is selected as the criterion for grid quality. Although the worst value of the minimum angle decreases from 44° to 25° during the ablation process, it is still far away from the failure criterion, i.e., 5°. For the CFD mesh, the orthogonal quality is selected as the criterion [41]. It can be found that the lowest orthogonal quality is 0.73 while the failure criterion is 0.1. Meanwhile, the maximum grid spacing along the coupling wall around the ablation pit is maintained as the initial state (1×10^{-6} m) during the ablation process. In conclusion, although the mesh quality would decrease to a certain degree in the ablation process due to the significant change of coupling interface, the quality of the CSD and CFD meshes can be preserved by utilizing the modified ALE adaptive mesh reconstruction method.

5.2.4. Comparison of ablation profile between numerical and experiment results

To validate the reliability of the developed coupled model, the simulated ablation profile is compared with the experimental results. Two types of experiments are chosen: (1) Experiment 1, which is corresponding to the analysis case in this paper, was conducted in the short-time hypersonic airflow condition [15]; (2) Experiment 2 was conducted in the long-time hypersonic airflow condition [16]. According to the numerical results, Fig. 10 (a1) and (b1) depict the time evolution of profiles over the surface and it can be clearly seen that the asymmetric ablation pits dynamically evolve around the laser spot center. Moreover, as shown in Fig. 10 (a2) and (b2), the simulated final ablation profile, i.e., the black solid line is compared with the experimental results, i.e., the red dash line in the figure. Qualitatively, it can be observed that the predicted results have a good agreement with the available experimental data on the ablation profile. Qualitatively, it can be observed that the predicted results have a good agreement with the available experimental data on the ablation profile. Quantitatively, the predicted maximum depth at the ablation center is slightly larger than the experiment data (simulation 1: 1180 μm, experiment 1: 1064 μm; simulation 2: 1794 μm, experiment 2: 1750 μm). The reasons may include the simplifications of load and boundary conditions in numerical model, the measurement errors in experiment test et al. Notwithstanding, the present work focuses on the development of coupled analysis approaches, it suggests that the coupling simulation results are reasonably accepted, and the

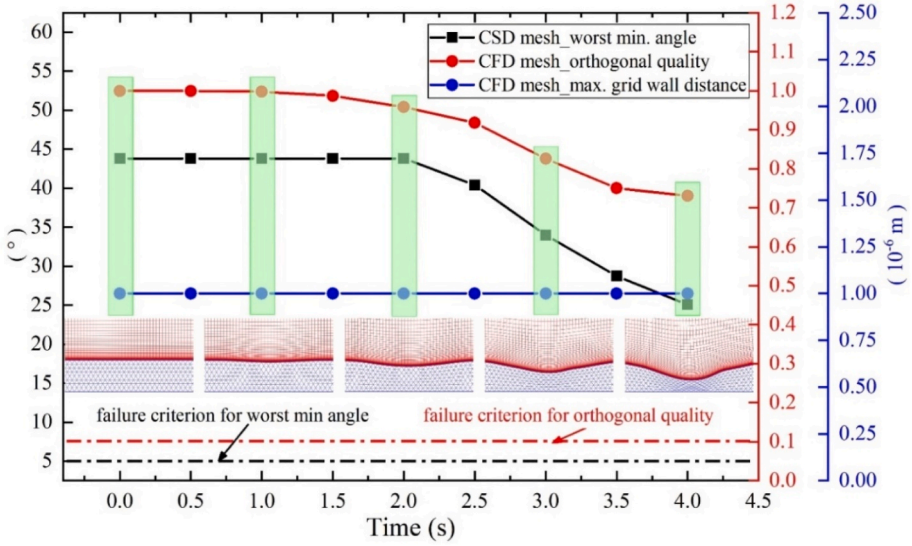

Fig. 9. Time evolution of mesh quality for both solid and fluid domains during the ablation process.

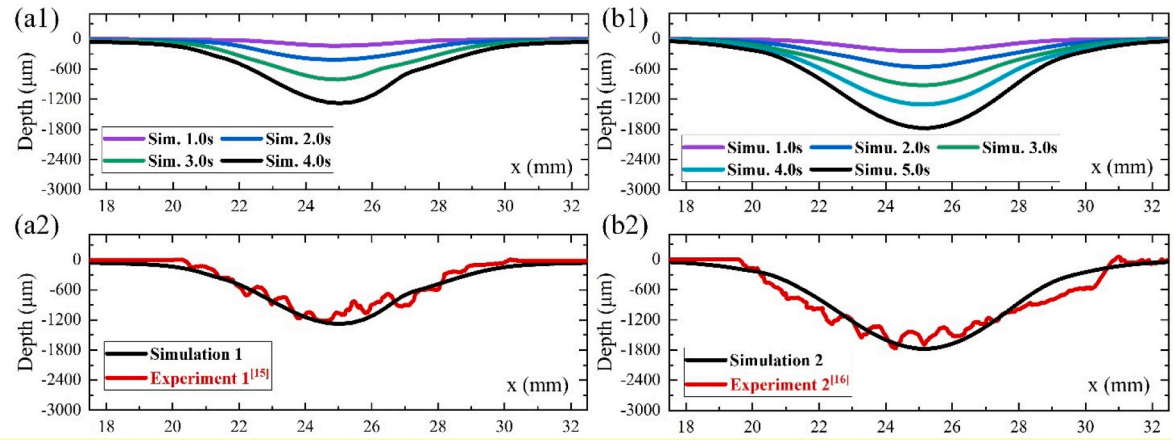

Fig. 10. Comparison between the predicted profile and experiment data.

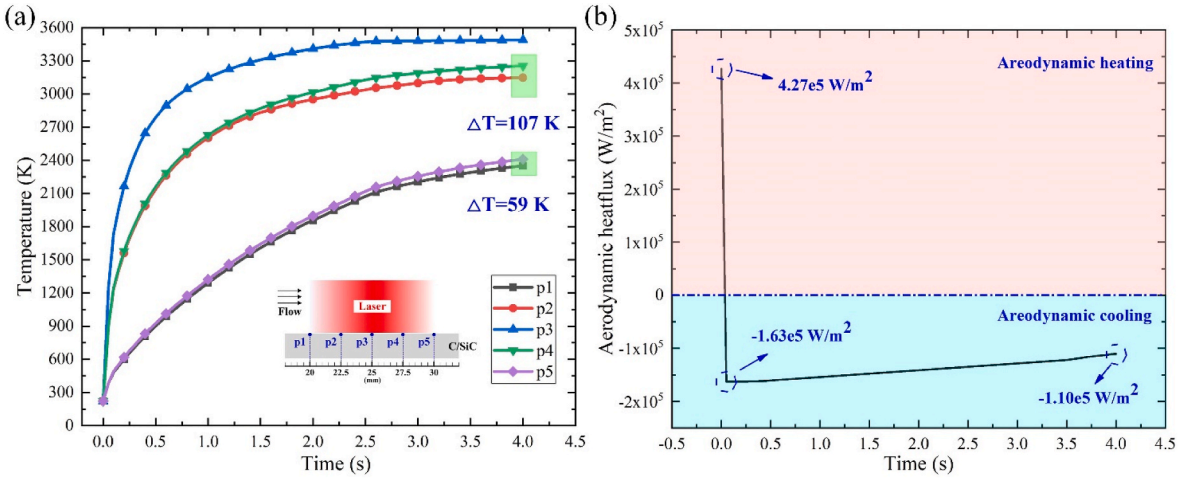

Fig. 11. Time evolution of (a) wall temperatures at different locations, and (b) aerodynamic heat flux on at the laser spot center.

proposed coupled model is reliable predict the laser ablation performance of composite structure subjected to high-speed airflow.

5.3. Localized multiphysics responses

Based on the established coupled model, the transient multiphysics responses can be captured. Just as illustrated in Movie 1, the overall localized multiphysics responses, including the evolutions of the static pressure and structural temperature around the ablation pit are firstly given. Then, the detailed multifield responses can be described and explained as follows.

Supplementary video related to this article can be found at

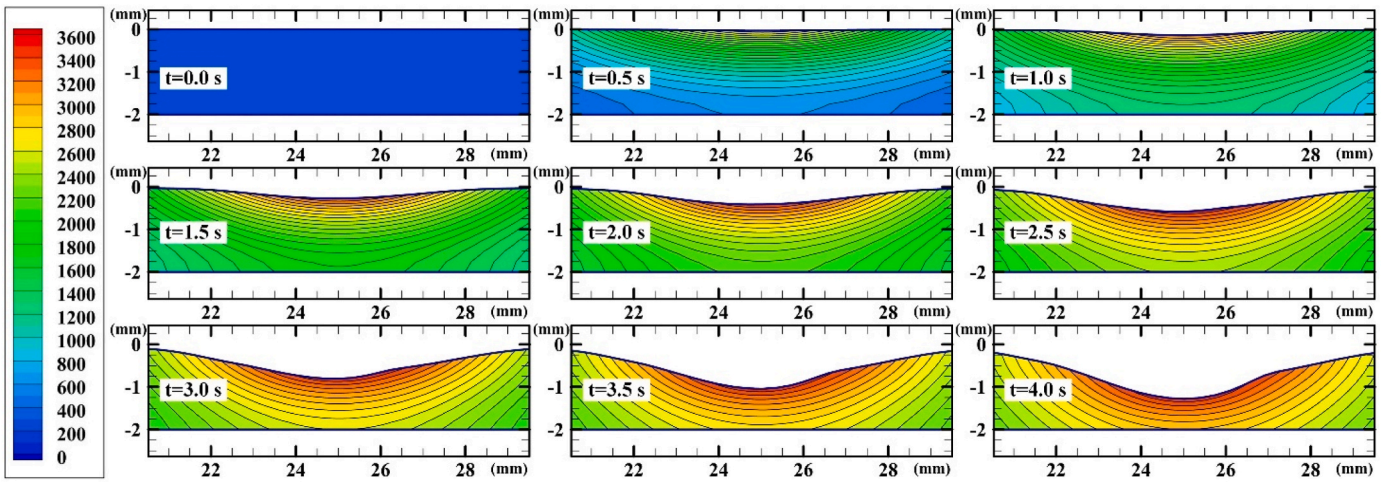

Fig. 12. Temperature contours of the solid domain at different times.

https://doi.org/10.1016/j.ijthermalsci.2023.108174

5.3.1. Structural temperature around the ablation pit

Fig. 11(a) shows the time evolution of structural temperature at different locations. As expected, the temperature continues to rise over the time period and the temperature at the laser spot center, i.e., p1, could approach 3490 K. However, the increase of wall temperature can reversely augment the heat flux that would be taken away from the solid domain through the enhancement of radiation, heat convection as well as sublimation. Thus, the temperature rise rate gradually slows down and a state of thermal equilibrium would be eventually reached if the irradiation time is prolonged enough. Just as shown in this figure, the temperatures at p2, p3 and p4 reach the equilibrium temperature and remain nearly constant after 3.0 s. However, the temperatures at p1 and p5, which are relatively far from the laser spot, have not reach the equilibrium state at the end of the laser radiation as extra time is needed to make the heat transfer stable in these areas. Moreover, it can be observed that the temperatures at the symmetric positions (i.e., p1/p5 and p2/p4) are different, and the temperature differences at 4.0 s of p1/p5 and p2/p4 are 107 K and 59 K, respectively. The asymmetric responses are mainly due to the asymmetric heat convection effect caused by the high-speed airflow.

In addition, it is interesting to observe that the aerodynamic heating effect would transform into aerodynamic cooling effect around the laser irradiation region as the wall temperature exceeds the recovery temperature of the hypersonic airflow during the radiation process. For example, as shown in Fig. 11(b), the aerodynamic heat flux at the laser spot center sharply decreases from 4.27e5 W/m^2 to −1.63e5 W/m^2 due to the rapidly increased wall temperature caused by the high-intensity laser heat flux. Then, the aerodynamic cooling effect gradually decreases from −1.63e5 W/m^2 to −1.10e5 W/m^2 as the ablation process goes on. One of the main reasons is that the heat transfer coefficient decreases due to the low-speed circulation region inside the localized ablation pit, which will be described in the next section.

Moreover, Fig. 12 illustrates the temperature contours of the solid domain at different times. It can be found that the high temperature concentrates around the laser irradiation region and the temperature tends to decline from the laser ablation interface into the solid domain. It can be also clearly seen that, as the laser irradiation time goes on, the laser heat flux gradually transfers to the depth of the structure through the coupling interface, and the heat transfer presents multi-dimensional characteristics.

5.3.2. Influence of localized ablation pit on the flow characteristics

The influence of the shape change of localized ablation pit on the flow characteristics are investigated in this section. The time evolution of the static pressure contours (Fig. 13), as well as the flow velocity contours and streamlines (Fig. 14) around the ablation pit are illustrated. It can be observed that flow phenomenon similar to the traditional cavity flow [49] occurs as the ablation pit evolves. We call it "pit flow" in this paper. Typically, two distinct flow structures are distinguished in the pit flow as time goes on.

The first flow regime, which is defined as the closed pit flow, emerges when the laser irradiation time is less than 2.0 s. The freestream would expand at the descent stage of the pit, and then be compressed at the ascent stage of the pit. Correspondingly, as typically shown in Fig. 13 (c), the pressure would firstly decrease below the ambient, then climb to peak at the downstream locations, and finally decrease to the ambient. Meanwhile, the evolution of the corresponding expansion waves and compression waves can be clearly observed in Fig. 13(a)–(c). Specially, as the ablation pit is relatively shallow at this time, the flow attaches to the wall all along, and neither the flow separation nor the vortices would be induced, just as shown in Fig. 14(a)–(c).

Subsequently, as shown in Fig. 14(d), the second flow regime, which is defined as the open pit flow, emerges after 2.0 s. In this case, large regions of low-speed circulation would be gradually generated inside the pit (Fig. 14(e)–(i)). In this case, the freestream flow does not enter the pit directly, and a shear layer is formed between the freestream and the flow inside the pit. The shear layer spans the length of the pit and impinges on the aft wall, which will cause server flow compression and high intensity static pressure. The typical static pressure distribution along the wall can be described as five stages: 1) decrease below the ambient at the lead edge area, 2) increase, 3) keep nearly uniform, 4) climb to peak on the aft wall, 5) decrease to the ambient, just as shown in Fig. 13 (i).

To distinguish the pit flow from the traditional cavity flow, the comparison between the two flows is conducted in Fig. 15. The differences can be described as follows.

(1) The closed flow regimes are different. The morphology of the ablation pit is much smoother than that of the traditional rectangular cavity. Thus, the flow in the closed pit always attaches on the wall, and the flow separation on the leading edge as well as

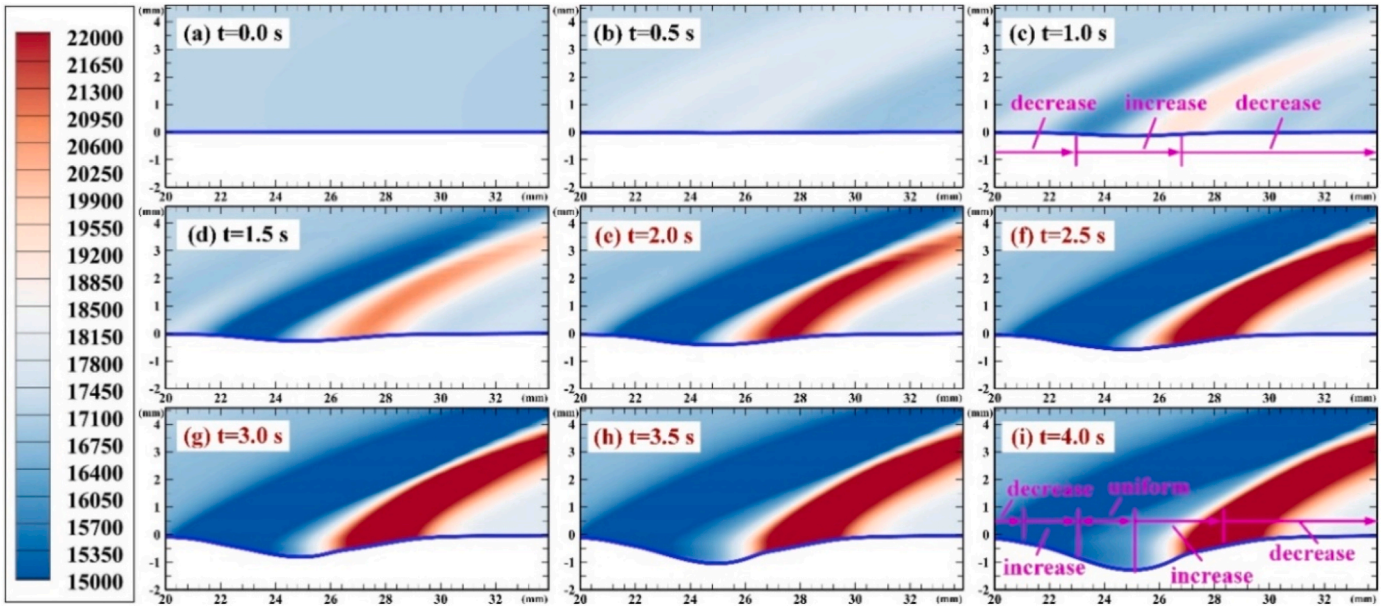

Fig. 13. Time evolution of static pressure contours around the localized ablation pit.

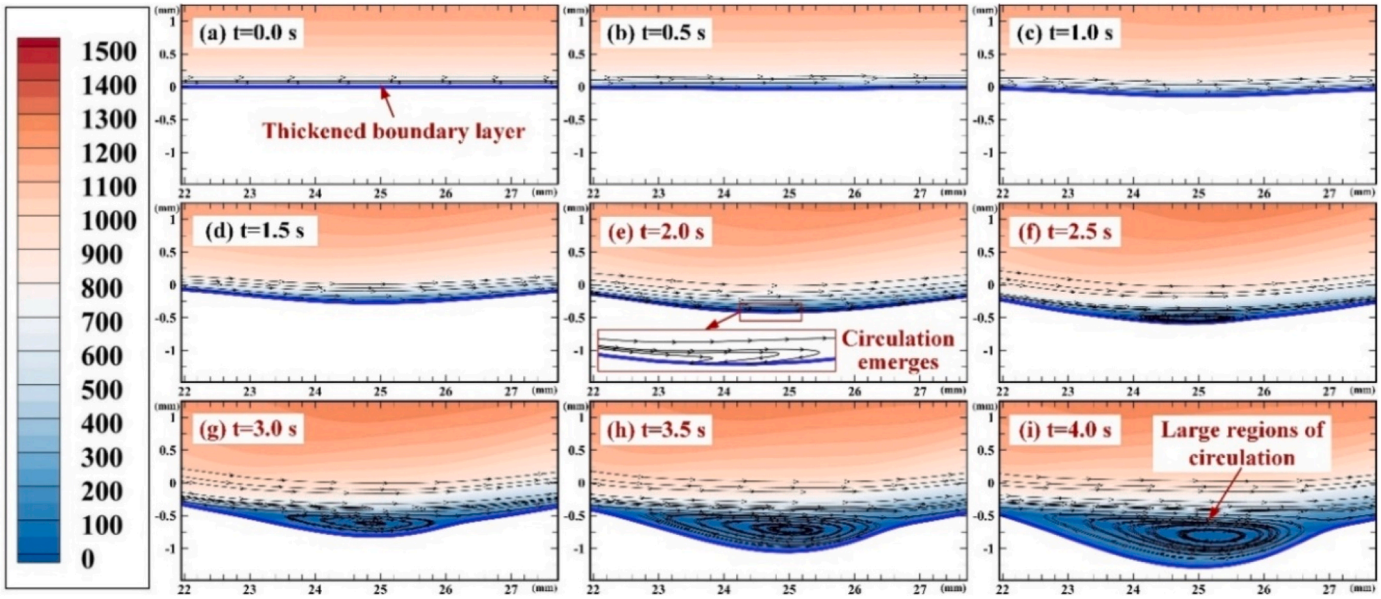

Fig. 14. Time evolution of flow velocity contours and streamlines around the localized ablation pit.

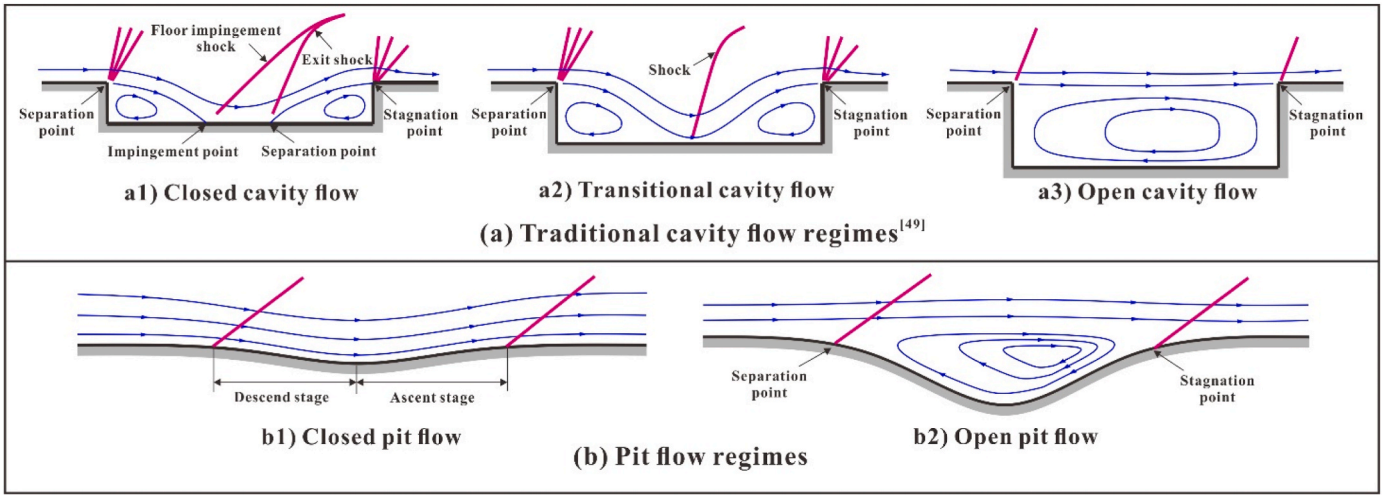

Fig. 15. Comparison of the different flow regimes. (a) The traditional cavity flow regimes; (b) The unique pit flow regimes.

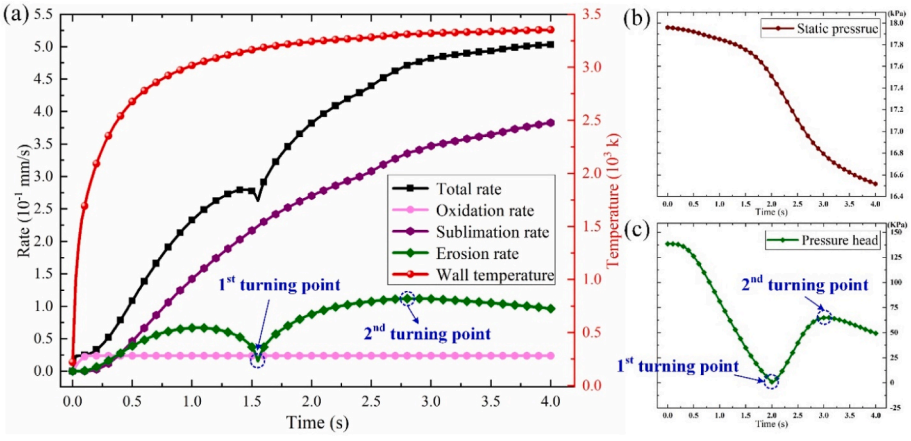

Fig. 16. Influence of localized flow characteristics on the ablation process. (a) Recession rates of different mechanisms; Time evolution of (b) the static pressure and (c) the dynamic pressure.

the flow impingement and separation on the floor in the closed cavity flow does not occur in the closed pit flow.

(2) Only two distinct regimes exist in the pit flow while three regimes exist in the cavity flow. The high wall temperature during the ablation process would increase the viscosity of the air near the wall, which makes the change of the fluid velocity harder. Under this circumstance, the velocity gradient near the wall decreases and the velocity distribution in the boundary layer is more even [50], which would notably thicken the boundary layer (Fig. 14 (a)) and accelerates the formation of the circulation. Consequently, the closed flow turns into the open flow directly as the pit gets deeper and the transitional state does not exist in the pit flow.

5.3.3. Influence of localized flow characteristics on different ablation mechanisms

The influence of the localized pit flow characteristics on each ablation mechanism is investigated in this section. As shown in Fig. 16 (a), the instantaneous contributions of different ablation mechanisms at the center of the C/SiC composite plate are firstly given. It can be clearly seen that the sublimation has the most important contribution to total recession rate, the following is the mechanical erosion, and the last is the oxidation reaction. Through the time integrating of the rates over the whole period, the contributions of sublimation, mechanical erosion, oxidation on the total ablation depth can be calculated and account for 64.4%, 29.1%, 6.5%, respectively.

For the sublimation reaction, the rate is closed related to the wall temperature and local static pressure according to the ablation model in Ref. [40]. As shown by the brown solid line in Fig. 16 (a), the sublimation rate keeps growing during the whole process. The reasons for this are twofold: the increasing wall temperature caused by the laser irradiation and the decreasing static pressure (Fig. 16 (b)) caused by the flow in the evolving pit. For the mechanical erosion, the rate lies on the wall temperature and dynamic pressure. The combing effect of the two factors results in the high nonlinearity of the erosion rate, just as shown by the green solid line in Fig. 16 (a). Note that, the two turning points of the erosion rate are corresponding to those of the dynamic pressure (Fig. 16 (b)) as the erosion rate positively correlates with the dynamic pressure. Obviously, the first turning point is due to the change of the pit flow regimes. And the second turning point is due to the decreased velocity around the center location, which is caused by the downstream movement of the stagnation point as the pit evolves, as shown in Fig. 14. For the oxidation reaction, two regimes can be observed. The first one is the kinetic regime, in which the oxidation reaction is reaction-limited and the recession rate sharply increases as the wall temperature quickly rises. The latter one is the diffusion regime, in which the recession rate magnitude is stable and mainly determined by the rates of diffusion of oxidizers to the surface, which depends on the pit flow characteristics.

Based on the above, it can be concluded that the localized pit flow has a significant impact on the ablation mechanisms, and the influence can be quantitatively investigated by utilizing the proposed coupling method.

6. Conclusion

In the paper, a coupled analysis model for the laser ablation behavior of composite structure in high-speed airflow is developed to reasonably assess the localized interaction effects of different physical fields. Numerical simulations on the laser ablation process of C/SiC composite plate subjected to the hypersonic airflow have been conducted and the localized coupling effects are carefully revealed. The main conclusions are summarized as follows.

(1) The fluid-thermal-ablation coupling framework integrating individual discipline solvers, coupling strategy, date exchange, mesh deformation is established. Here a loosely coupled scheme with extrapolation-based predictors is developed to maintain the second-order temporal accuracy, and the effects of the coupling step is discussed. For the case in this work, the coupling time step of 0.05 s is chosen to balance the accuracy and efficiency. And a mesh deformation method combining ALE algorithm and RBF interpolation algorithm is presented to achieve the localized surface recession by high quality mesh reconstruction. Results show that the quality of the CSD and CFD meshes can be preserved during the ablation process. Moreover, by comparison, the predicted ablation profile agrees well with the available experimental result, which demonstrates the validity of the proposed coupling analysis framework.

(2) The localized coupling effects between the laser ablation behavior of C/SiC composite and hypersonic airflow are fully investigated. On the one hand, results show that the evolution of the localized ablation pit would induce the transient of two distinct pit flow regimes, namely from the closed pit flow to the open pit flow. The characteristics of different pit flow regimes are carefully revealed. On the other hand, the influence of the localized pit flow characteristics on each ablation mechanism of composite structure is investigated. We demonstrate that the flow regime transition would remarkably change the localized flow characteristics, including the local static pressure and dynamic pressure, which in turn significantly affects the sublimation and mechanical erosion rates of C/SiC composite plate, respectively.

Generally, the details of multifield responses can be reliably predicted by the proposed method, which lays a preliminary foundation for the localized coupling effects analysis of the laser ablation behavior of different composite structures subjected to high-speed airflow. In the future work, the numerical modeling of the interaction effects between the ablation products and the high-speed airflow will be further considered, and more experimental studies will be conducted to validate the coupling analysis model comprehensively.

Declaration of competing interest

The authors declare that they have no known competing financial interests or personal relationships that could have appeared to influence the work reported in this paper.

Data availability

Data will be made available on request.

Acknowledgement

Financial supports from National Natural Science Foundation of China (Grant Nos. 11902322, 11972035 and 11972033) are gratefully acknowledged.

Appendix A. Supplementary data

Supplementary data to this article can be found online at https://doi.org/10.1016/j.ijthermalsci.2023.108174.

Appendix A. Ablation model for C/SiC composites under high-speed airflow

In the paper, the ablation model in Ref. [40] is adopted to determine the recession rate of C/SiC composites. The total recession rate can be expressed as follows:

$$r_{total} = \frac{\dot{m}}{\rho_w} = r_c + r_s + r_e \tag{A1}$$

where r_c, r_s and r_e denote the recession rates of chemical reaction of oxidization, sublimation and thermomechanical erosion, respectively; ρ_w is the density on the ablation surface. Note that, for C/SiC composite, the internal erosion is ignored as no pyrolysis reaction occurs. Therefore, only the external erosion caused by the external hypersonic airflow should be considered.

A1. Sublimation

Due to the high intensity of heat flux induced by laser, the sublimation of carbon fiber and SiC matrix inside composites occurs during the ablation progress. The reactions can be described as:

$$3C_{(s)} \rightarrow C_{3(g)} \tag{A2}$$

$$SiC_{(s)} \rightarrow SiC_{(g)} \tag{A3}$$

Then, the sublimation rate of either component can be described by:

$$r_{s,i} = \frac{1}{\rho_w}\left(h_c/C_p\right)\left(p_g^*/p_e\right)\exp\left(-\frac{E_{i,s}}{RT_w}\right) \tag{A4}$$

where h_c is the convective heat transfer coefficient, C_p is the specific heat capacity at constant pressure, p_e is the local pressure of airflow, p_g^* is the constant characterizing a pressure of 'initial state' of the generated gas phase, $E_{i,s}$ is the activation energy of the sublimation reaction, and R is the ideal gas constant, 8.314 J/(mol•K).

Consequently, r_s can be expressed as the sum of the sublimation rates of fiber and matrix:

$$r_s = r_{s,C} + r_{s,SiC} \tag{A5}$$

A2. Chemical reaction of oxidization

For C/SiC composites, the oxidation of carbon fiber and SiC matrix in oxygen is mainly considered. Specially, in this work, the rection of SiC matrix is mainly dominated by active oxidation for the low pressure and high temperature. Thus, the reactions can be described as follows:

$$2C + O_2 = 2CO \tag{A6}$$

$$SiC + O_2 = SiO + CO \tag{A7}$$

For the oxidation reaction of C/SiC, it is controlled by the reactive regime and diffusive regime. According to the Arrhenius thermochemical kinetic formula, the linear oxidation rate under kinetic reaction control mechanism can be described by:

$$r_{\mathrm{react},i} = \frac{\dot{m}_i}{\rho_w} = \frac{1}{\rho_w}\frac{aM_i}{M_{O_2}}A_{i,O}\exp\left(-\frac{E_{i,O}}{RT_w}\right)P_{Ow} \tag{A9}$$

where a is the coefficient of the reaction equation, M_i is the molecular mass, M_{O_2} is the relative molecular mass of oxygen, $E_{i,O}$ and $A_{i,O}$ are the activation energy and pre-exponential factor respectively, P_{Ow} is the partial pressure of oxygen at ablation surface.

The ablation rate under diffusion control mechanism can be described by:

$$r_{\mathrm{diffision},i} = \frac{1}{\rho_w}\frac{h_c}{C_p}\frac{aM_i}{M_{O_2}}\omega_{O_2} \tag{A10}$$

where ω_{O_2} is the mass concentration of oxygen in the airflow.

Consequently, the actual oxidation rate should be the minimum of the rate under the reactive regime and diffusive regime according to the minimum control model as follows:

$$r_c = \min\left(v_{O-\mathrm{react}}, v_{O-\mathrm{diffusion}}\right) \tag{A11}$$

A3. Thermomechanical erosion

According to Ref. [40], the linear rate of thermomechanical erosion is related to the external thermomechanical erosion rate of matrix and fiber. And the erosion rate of matrix and fiber can be written as follows:

$$r_m = \frac{1}{\rho_m}\left(\frac{J_m^0 k_m}{c_m}\right)^{0.5}\left(\frac{6p_v}{\sigma_{mT}}\right)^{0.33}\left(\frac{RT_w}{E_{Am}}\right)^{0.5}\exp\left(-\frac{E_{Am}}{2RT_w}\right) \tag{A12}$$

$$r_{f,trans} = \frac{1}{\rho_f}\left(\frac{J_f^0 k_f}{c_f}\right)^{0.5}\left(\frac{6p_v}{\sigma_{f,trans}}\right)^{0.33}\left(\frac{RT_w}{E_{Af}}\right)^{0.5}\exp\left(-\frac{E_{Af}}{RT_w}\right) \tag{A13}$$

$$r_{f,longi} = r_{f,trans}\left(\frac{\sigma_{f,trans}}{\sigma_{f,longi}}\right)^{0.5} \tag{A14}$$

where $r_{f,trans}$ and $r_{f,longi}$ are the rates of external thermomechanical erosion of fibers in transverse and longitudinal directions; k_f, ρ_f, c_f and k_m, ρ_m, c_m are heat-physical characteristics of the fibers and matrix; J_f^0, E_{Af} and J_m^0, E_{Am} are pre-exponential multiplier and activation energy of thermodecomposition process; σ_{mT} is the strength of matrix in tension, $\sigma_{f,longi}$ and $\sigma_{f,trans}$ are the strength of carbon fibers in the longitudinal and perpendicular directions.

For transversally isotropic composites, there exist two different components about ablation rate of erosion:

$$\begin{cases} r_e = r_{e1}\left({n_1}^2 + {n_2}^2\right) + r_{e2}{n_3}^2 \\ r_{e1} = \left(\dfrac{1-\delta_m}{r_{f,trans}} + \dfrac{\delta_m}{r_m}\right)^{-1} \\ \delta_m = \dfrac{h_m}{h_m + h_f} \\ r_{e2} = r_{f,longi} \end{cases} \tag{A15}$$

where r_{e1} is the rate of the surface orthogonal to the n_3 axis (thickness direction); r_{e2} is the rate of the surface orthogonal to the axis n_1 and n_2 (in-plane direction); δ_m is the relative thickness of the matrix interlayer between the layers of fibers in the unidirectional composite; h_m and h_f is the thicknesses of the layers of the matrix and fiber.

References

[1] P. Parandoush, A. Hossain, A review of modeling and simulation of laser beam machining, Int. J. Mach. Tool Manufact. 85 (2014) 135–145.
[2] M. Dal, R. Fabbro, An over view of the state of art in laser welding simulation, Opt Laser. Technol. 78 (2016) 2–14.
[3] P. Sprangle, B. Hafizi, A. Ting, R. Fischer, High-power lasers for directed-energy applications, Appl. Opt. 54 (31) (2015) 201–209.
[4] P.Y. Nan, Z.H. Shen, B. Han, X.W. Ni, The influences of laminated structure on the ablation characteristics of carbon fiber composites under CW laser irradiation, Opt Laser. Technol. 116 (2019) 224–231.
[5] W.J. Li, H.M. Huang, Y. Tian, Z. Zhao, A nonlinear pyrolysis layer model for analyzing thermal behavior of charring ablator, Int. J. Therm. Sci. 98 (2015) 104–112.
[6] L. Geng, X.C. Liu, Q.G. Fu, S. Cheng, H.J. Li, Laser ablative behavior of C/C modified by Si reactive infiltration, Carbon 168 (2020) 650–658.
[7] Y.G. Tong, S.X. Bai, H. Zhang, Y. Ye, Laser ablation behavior and mechanism of C/SiC composite, Ceram. Int. 39 (2013) 6813–6820.
[8] J. Chen, Q.L. An, W.W. Ming, M. Chen, Investigations on continuous-wave laser and pulsed laser induced controllable ablation of SiCf/SiC composites, J. Eur. Ceram. Soc. 41 (2021) 5835–5849.
[9] X.L. Dang, X.W. Yin, X.M. Fan, Y.H. Ma, J.T. Wang, P.F. Ju, H.W. Song, Microstructural evolution of carbon fiber reinforced SiC-based matrixcomposites during laser ablation process, J. Mater. Sci. Technol. 35 (2019) 2919–2925.
[10] B. Sinkovics, P. Gordon, G. Harsanyi, Computer modelling of the laser ablation of polymers, Appl. Therm. Eng. 88 (2015) 410–417.
[11] K. Zhukovsky, D. Oskolkov, Modeling of heat transport and exact analytical solutions in thin films with account for constant non-relativistic motion, Int. J. Heat Mass Tran. 150 (2020), 119085.
[12] Y.Q. Wang, C.L. Pasiliao, Modeling ablation of laminated composites A novel manual mesh moving finite element analysis procedure with ABAQUS, Int. J. Heat Mass Tran. 116 (2018) 306–313.
[13] Y.Q. Wang, N.G. Shen, G.K. Befekadu, C.L. Pasiliao, Modeling pulsed laser ablation of aluminum with finite element analysis considering material moving front, Int. J. Heat Mass Tran. 113 (2017) 1246–1253.
[14] J.T. Wang, Y.Z. Ma, Y.W. Liu, W. Yuan, H.W. Song, C.G. Huang, X.W. Yin, Experimental investigation on laser ablation of C/SiC composites subjected to supersonic airflow, Opt Laser. Technol. 113 (2019) 399–406.
[15] Z. Wang, J.T. Wang, H.W. Song, W. Yuan, Y.W. Liu, T. Ma, C.G. Huang, Laser ablation behavior of C/SiC composites subjected to transverse hypersonic airflow, Corrosion Sci. 183 (2021), 109345.
[16] Z. Wang, R.X. Wang, H.W. Song, T. Ma, J.T. Wang, W. Yuan, C.G. Huang, Decoupling mechanisms of "avalanche" phenomenon for laser ablation of C/SiC composites in hypersonic airflow environment, Int. J. Therm. Sci. 173 (2022), 107414.
[17] Y.H. Huang, H.W. Song, C.G. Huang, Heat transfer and mode transition for laser ablation subjected to supersonic airflow, Chin. Phys. Lett. 33 (1) (2016), 014201.
[18] H.M. Jiang, G.M. Zhao, M.S. Chen, L.G. Jiao, J.S. Li, Laser irradiation effects on metal or composite plates subjected to surface flow, in: Proc. SPIE 8796, 2nd International Symposium on Laser Interaction with Matter, LIMIS 2012, 2013, 879603.
[19] M.P. Bacos, J.L. Cochon, J.M. Dorvaux, O. Lavigne, C/C composite oxidation model: II. Oxidation experimental investigations, Carbon 38 (1) (2000) 93–103.
[20] W.J. Li, H.M. Huang, X.L. Xu, A coupled thermal/fluid/chemical/ablation method on surface ablation of charring composites, Int. J. Heat Mass Tran. 109 (2017) 725–736.
[21] Y.I. Dimitrienko, I.D. Dimitrienko, Effect of thermomechanical erosion on heterogeneous combustion of composite materials in high-speed flows, Combust. Flame 122 (3) (2000) 211–226.
[22] D.Y. Deng, J.J. Yu, X.Q. Yan, F. Huang, X.G. Luo, Engineering method for the thermal mechanical erosion of C/C composite with the mesoscale ablation model, Polym. Polym. Compos. 22 (2014) 181–185.
[23] P.Y. Nan, X. Li, Y.X. Pan, Z.W. Li, Z.H. Shen, X.W. Ni, Characteristics and influences of plume during CW laser-CFRP interaction under tangential gas flow, Laser Phys. 30 (2020), 076003.
[24] J.G. Michopoulos, C. Farhat, J. Fish, Modeling and simulation of multiphysics systems, J. Comput. Inf. Sci. Eng. 5 (2005) 198–213.
[25] F. Chen, H. Liu, S.T. Zhang, Time-adaptive loosely coupled analysis on fluid-thermal-structural behaviors of hypersonic wing structures under sustained aeroheating, Aero. Sci. Technol. 78 (2018) 620–636.
[26] R.X. Wang, Z.W. Wang, H.W. Zheng, H.W. Song, Comparison of strategies for coupled flow-thermal analysis of thermal protection system at hypersonic flight condition, Int. J. Aeronaut. Space 21 (2020) 347–362.
[27] B.A. Miller, J.J. McNamara, Efficient fluid-thermal-structural time marching with computational fluid dynamics, AIAA J. 56 (9) (2018) 3610–3621.
[28] B.A. Miller, J.J. McNamara, Time-marching considerations for response prediction of structures in hypersonic flows, AIAA J. 53 (10) (2015) 1–11.
[29] F. Chen, H. Liu, S.T. Zhang, Coupled heat transfer and thermo-mechanical behavior of hypersonic cylindrical leading edges, Int. J. Heat Mass Tran. 122 (2018) 846–862.
[30] K. Ye, Z.Y. Ye, C.N. Li, J. Wu, Effects of the aerothermoelastic deformation on the performance of the three-dimensional hypersonic inlet, Aero. Sci. Technol. 84 (2019) 747–762.
[31] A.J. Culler, J.J. McNamara, Impact of Fluid-thermal-structural coupling on response prediction of hypersonic skin panels, AIAA J. 49 (11) (2011) 2393–2406.
[32] J. Huang, P. Li, W.X. Yao, Thermal protection system gap analysis using a loosely coupled fluid-structural thermal numerical method, Acta Astronaut. 146 (2018) 368–377.
[33] D.B. Han, J.S. Kim, K.H. Kim, Conjugate thermal analysis of X-51A-like aircraft with regenerative cooling channels, Aero. Sci. Technol. 126 (2022), 107614.
[34] X.W. Sun, H.B. Yang, T. Mi, Thermo-structural behaviour prediction of the nose cap of a hypersonic vehicle based on multifield coupling, Int. J. Aerospace Eng. 2020 (2020), 3850283.

[35] P. Schrooyen, A. Turchi, K. Hillewaert, P. Chatelain, T.E. Magin, Two-way coupled simulations of stagnation-point ablation with transient material response, Int. J. Therm. Sci. 134 (2018) 639–652.
[36] D. Bianchi, F. Nasuti, E. Martelli, Navier-Stokes simulations of hypersonic flows with coupled graphite ablation, J. Spacecraft Rockets 47 (4) (2010) 554–562.
[37] A. Martin, I.D. Boyd, Strongly coupled computation of material response and nonequilibrium flow for hypersonic ablation, J. Spacecraft Rockets 52 (1) (2015) 89–104.
[38] W.J. Li, H.M. Huang, B.C. Ai, Z.M. Zhang, On the novel designs of charring composites for thermal protection application in reentry vehicles, Appl. Therm. Eng. 93 (2016) 849–855.
[39] S.H. Meng, Y.J. Zhou, W.H. Xie, F.J. Yi, S.Y. Du, Multiphysics coupled fluid/thermal/ablation simulation of carbon/carbon composites, J. Spacecraft Rockets 53 (5) (2016) 930–935.
[40] Y.I. Dimitrienko, Thermomechanics of Composite Structures under High Temperatures, Springer Netherlands, Dordrecht, 2016.
[41] ANSYS, ANSYS Fluent 16.0 Theory Guide, 2015.
[42] ABAQUS Documentation, Version 6.13, Dassault Systèmes Simulia Corp., Providence, RI, USA, 2014.
[43] M.D. Buhmann, Radial Basis Functions: Theory and Implementations, Cambridge University Press, Cambridge, 2009.
[44] T.C.S. Rendall, C.B. Allen, Fluid-structure interpolation and mesh motion using radial basis functions, Int. J. Numer. Methods Eng. 75 (10) (2008) 1519–1559.
[45] Z. Zhao, R. Ma, L. He, X.H. Chang, L.P. Zhang, An efficient large-scale mesh deformation method based on MPI/OpenMP hybrid parallel radial basis function interpolation, Chin. J. Aeronaut. 33 (5) (2020) 1392–1404.
[46] J.D. Anderson, Hypersonic and High-Temperature Gas Dynamics, AIAA, 2019.
[47] F.Y. Wang, L.F. Cheng, Q. Zhang, L.T. Zhang, Effect of surface morphology and densification on the infraredemissivity of C/SiC composites, Appl. Surf. Sci. 313 (2014) 670–676.
[48] Y.G. Tong, S.X. Bai, H. Zhang, Y.C. Ye, Laser ablation behavior and mechanism of C/SiC composite, Ceram. Int. 39 (2013) 6813–6820.
[49] S.J. Lawson, G.N. Barakos, Review of numerical simulations for high-speed, turbulent cavity flows, Prog. Aero. Sci. 47 (2011) 186–216.
[50] R. Zhao, C.Y. Wen, X.D. Tian, T.H. Long, W. Yuan, Numerical simulation of local wall heating and cooling effect on the stability of a hypersonic boundary layer, Int. J. Heat Mass Tran. 121 (2018) 986–998.